Seismic-to-well ties by smooth dynamic time warping

Tianci Cui and Gary F. Margrave

ABSTRACT

Without knowledge of Q or a check-shot/VSP survey, synthetic seismogram has to be manually stretched or squeezed to tie the seismic traces in practice, which is a tedious process and always involves human errors. Dynamic time warping (DTW) can reliably estimate the time shifts between two signals, but it returns unsmooth integer lags. The improved algorithm, smooth dynamic time warping (SDTW), can accurately estimate smooth time shifts, which are more realistic to represent the drift time in seismic-to-well ties. Taking the place of the interpretive stretch-squeeze process, SDTW is applied to estimate the time shifts between the synthetic seismogram and seismic traces of the Hussar field data. The estimated time shifts are used to calibrate the timing of the reflectivity instead of warping the synthetic seismogram, to reserve the embedded zero-phase wavelets but making the time calibration adequate only after two iterations. Both the residual drift time and overestimated sonic overburden cause theses time shifts, which have similar slops at the three well locations attributed from the flat subsurface geological structure in the Hussar area. The time-variant constant-phase difference and time-variant amplitude scalar function are calculated between the time calibrated synthetic seismogram and the seismic traces. They are linearly interpolated and extrapolated from the three wells to other CDP locations horizontally to rotate the phase and balance the amplitude of the whole seismic section. After seismic-to-well ties, the same well tops are tied to the same seismic events, making major seismic horizons easy to be identified. The bandlimited impedance inversion of the Hussar seismic data using a low-frequency cut-off of 3 Hz and a high-end frequency of 75 Hz is shown to be a good approximation to the subsurface properties. The second iteration of time calibration significantly reduces the percent errors around well 12-27 between the seismic inversion and well impedance, verifying better seismic-to-well ties.

SMOOTH DYNAMIC TIME WARPING

Cui and Margrave (2014a) use a technique called dynamic time warping (DTW) to estimate the drift time between a stationary synthetic seismogram calculated from well logs and a nonstationary seismic trace caused by anelastic attenuation at the well location. By tying two traces, dynamic time warping can estimate the time shifts between them using dynamic programming to solve a constrained optimization problem, but it returns unsmooth integer lags. Compton and Hale (2014) extend the dynamic time warping method to a smooth dynamic time warping (SDTW) algorithm to estimate smoother and more accurate time shifts. In this report, SDTW is compared to DTW and is applied to seismic-to-well ties.

Consider two synthetic traces $s_1(n)$ and $s_2(n)$ shown in Figure 1 top panel where $n = 1, 2, \dots, N$ is sample number. Trace $s_1(n)$ is computed by convolving a random reflectivity series with a minimum-phase wavelet whose dominant frequency is 30 Hz. Trace $s_1(n)$ is then warped by a time-variant shift sequence $tshift(n)$ to obtain trace $s_2(n)$. The maximum crosscorrelation coefficient between $s_1(n)$ and $s_2(n)$ is 0.4 and this occurs at a lag of -24.2 milliseconds (a negative lag value indicates s_2 is delayed relative to s_1). Time

shift sequence $tshift(n)$ is a sinusoidal function as shown in Figure 1 bottom panel. DTW and SDTW are adapted respectively to estimate the time shift sequence $nshift(n)$ expressed in lags given the traces $s_1(n)$ and $s_2(n)$.

Figure 2 is a zoomed-in part of the alignment error array e calculated for both DTW and SDTW, in which the alignment error values are denoted by different colors. With the constraint

$$|nshift(n) - nshift(n-1)| \leq 1, \quad (1)$$

DTW searches subpaths of only 3 slope values (-1, 0 and 1) shown in red lines, traveling across every two consecutive time samples. Thus, the globally optimal path (dotted white curve) calculated by DTW is the combination of subpaths with these 3 slopes. As we can see, it cannot well approximate the known lag sequence (solid white curve), which is smooth and has multiple slope values between -1 and 1. What is more, when traces s_1 and s_2 are not simply the time-shifted version of each other, the ability of DTW is in doubt to detect such minute time shift changes for every two consecutive time samples, whose interval can be tens times smaller than the time period of seismic events. In seismic-to-well ties, the drift time used to calibrate the timing difference between the sonic logs and the seismic should be smooth and varies slowly with two-way traveltime to reduce artificial events being introduced in the corrected seismic trace. And seismic traces are not related to synthetic seismograms by time shifts only, but also involve amplitude and phase changes in the presence of anelastic attenuation.

According to Compton and Hale (2014), SDTW can estimate a much smoother time shift sequence with as many possible slopes as required. It is more accurate than DTW especially when two traces are not related by time shifts only, but also have differences in waveforms, noise and etc. Instead of searching 3 possible subpaths at every single time sample, SDTW searches $2h + 1$ possible subpaths of multiple slope values ranging from -1 to 1 at every h^{th} sample. Figure 3 shows the same alignment error array and 11 subpaths of different slopes searched for the same sample location by SDTW as Figure 2 when the coarse sampling interval h equals 5 samples. Similar to DTW, alignment errors are then accumulated along each possible linear subpath across h samples, and the subpath with the minimal summation is locally optimal. For a sample on a subpath but at a noninteger lag, its alignment error value is approximated by linearly interpolating the alignment error values of its two vertically adjacent samples. The white circles in Figure 3 are the sample locations where the locally optimal subpaths are calculated. By piecewise-linearly interpolating these coarse samples, we obtain the globally optimal path (dotted white curve), which approximates the known lag sequence (solid white curve) much better than the one from DTW. When $h = 1$, SDTW is equal to DTW.

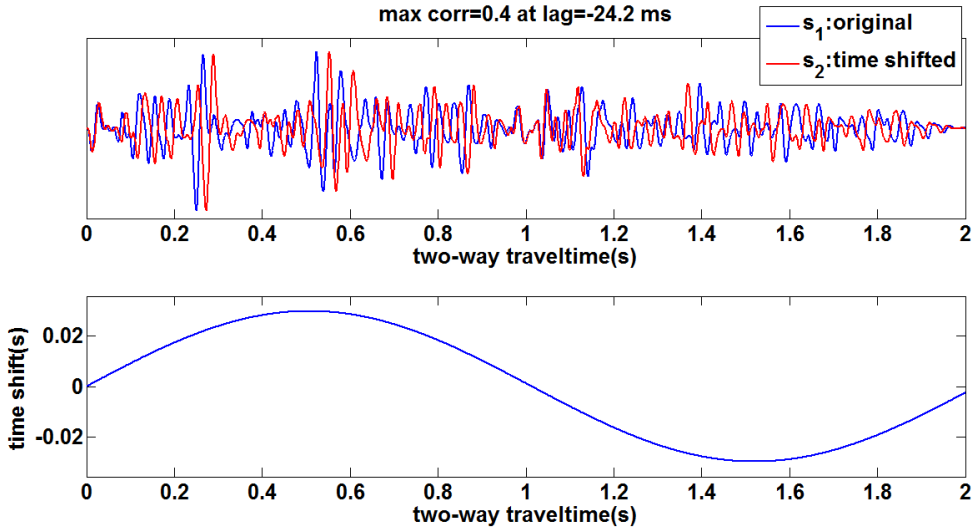

Figure 1: Two synthetic traces (top) and the time shift sequence between them (bottom).

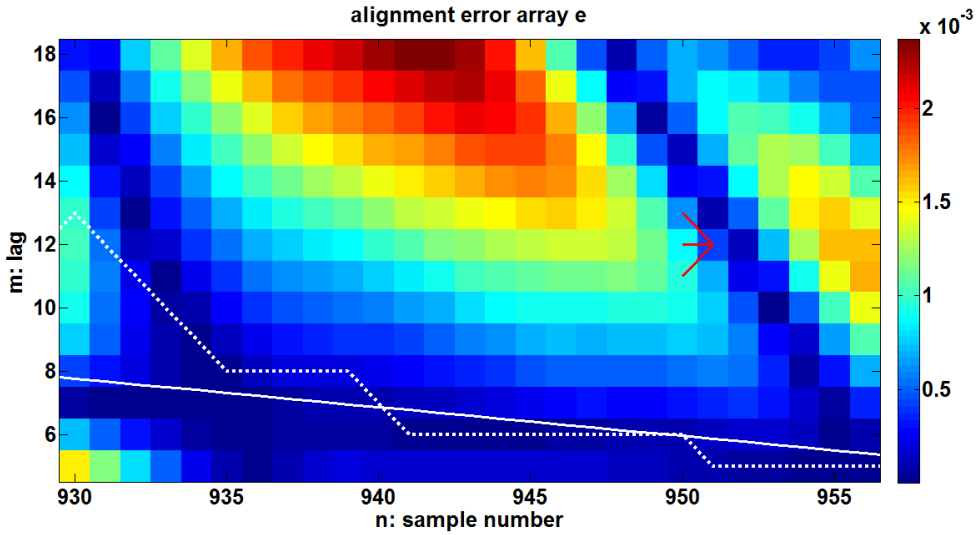

Figure 2: Zoomed-in part of alignment error array, on top of which are the 3 subpaths searched for a certain sample location in red lines, the known lag sequence in solid white curve and the estimated lag sequence by DTW in dotted white curve.

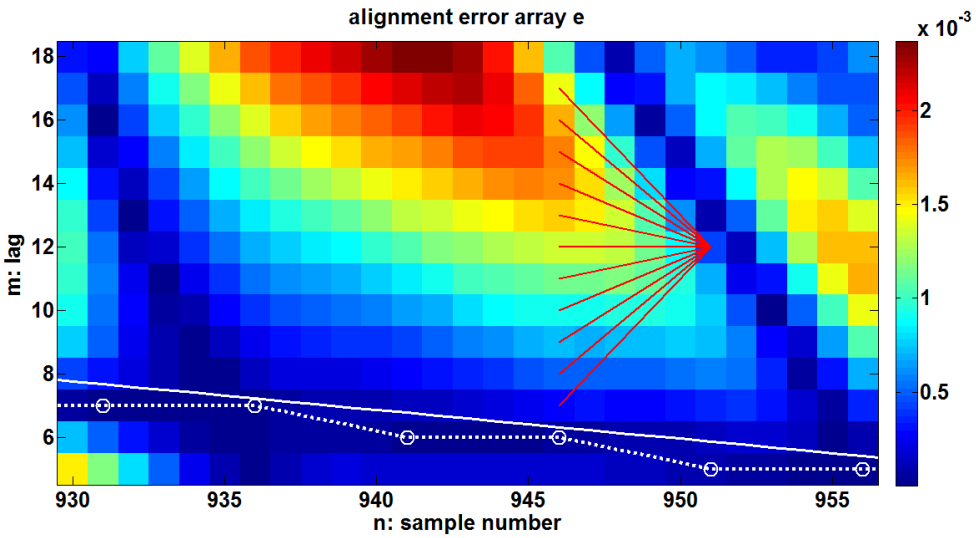

Figure 3: Zoomed-in version of alignment error array, on top of which are the 11 subpaths searched for a certain sample location in red lines, the known lag sequence in solid white curve, and the estimated lag sequence by SDTW in dotted white curve with white circles indicating the coarse sample locations where its subpaths are calculated.

SDTW searches locally optimal paths every h samples, ending up with a distance array h times smaller than the one accumulated by DTW, which saves computation time and memory significantly. Numerical tests (not shown here) find that in this case, SDTW does a good job when the value of h is about 100. If h is too small, the estimated time shifts are not smooth enough. If h is too large, the globally optimal path is composed by only limited number of linear subpaths, which cannot well approximate the known time shifts. Furthermore, different distributions of the coarse samples result in similar estimates as long as they are approximately 100 samples apart. Figure 4 shows the distance array accumulated by SDTW when $h = 100$. Compared to the distance array calculated by DTW in Figure 2 or 3, SDTW loses horizontal resolution because it estimates time shifts at coarsely sampled locations only, making the estimated time shift sequence (solid white curve) smoother and more robust when differences other than time shifts exist between two traces. Figure 5 top panel compares the known time shift sequence in solid blue curve, the estimate by SDTW when $h = 100$ in solid red curve with red circles indicating the coarse locations with 100 samples apart where the time shifts are calculated, and the estimate by DTW after being convolved with a normalized Gaussian window with 100 ms half-width in dotted black curve. The time shift sequence estimated by DTW is smoothed and better approximates the known time shifts, but it remains obviously erroneous from 0.6 to 0.8 s. Thus, smoothing the rough time shifts estimated by DTW is not equal to the globally optimal time shifts computed by SDTW. Trace s_1 is warped by the SDTW estimated time shifts and the time shifted trace (solid blue curve in Figure 5 bottom panel) is well tied to trace s_2 (dotted red curve in Figure 5 bottom panel). The maximum crosscorrelation coefficient between them is 0.98 at a lag of 0.1 milliseconds, indicating a superb correlation.

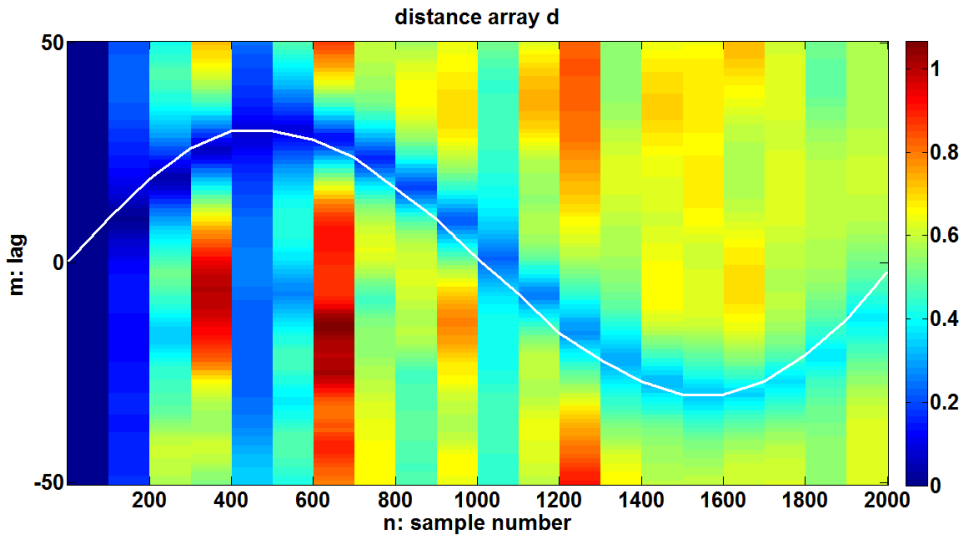

Figure.4: Distance array accumulated every 100th sample. The lag sequence calculated by SDTW is plotted in white on top of the distance array.

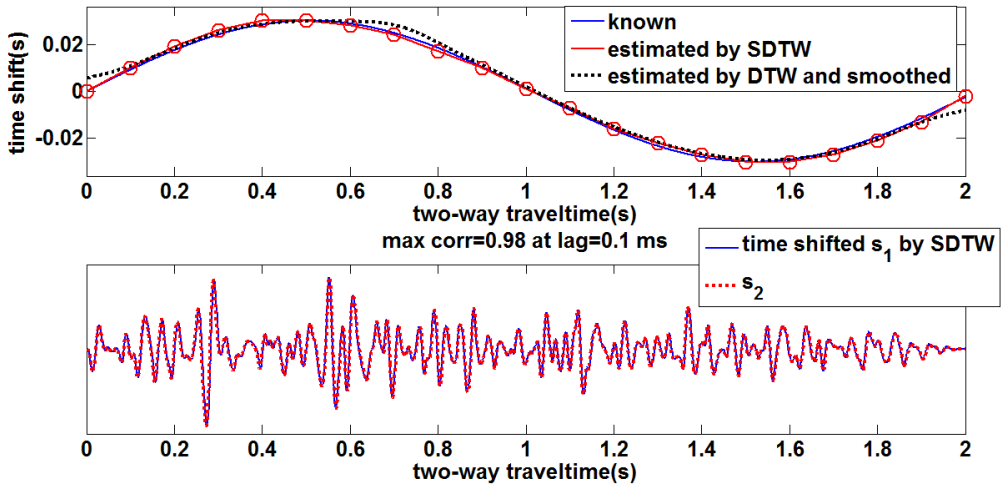

Figure 5: Known and estimated time shift sequences (top). Time shifted s_1 by SDTW in comparison with s_2 (bottom).

COMPARISON WITH TIME-VARIANT CROSSCORRELATION

The common method, time-variant crosscorrelation (TVCC) is also applied to estimate the time shifts between traces s_1 and s_2 for comparison with DTW and SDTW. Without knowledge of $tshift$, TVCC can estimate it at every Gaussian window center time τ via

$$tshift_{est} = \arg\max_{t} (s_1^{\sigma} \otimes s_2)(t) \quad (2)$$

where $\otimes$ denotes crosscorrelation over time t. Equation 2 means that trace s_1 is windowed by a sliding Gaussian function of standard width 2σ centered at time τ and the estimated time shift corresponding to τ is the time lag at which the crosscorrelation coefficient between s_1^{σ} and s_2 is maximum. In this case, the Gaussian window is chosen to have a half-width of 100 ms and an increment of 10 ms. The estimated time shift function $tshift_{est}$ is plotted in dotted red in Figure 6 top panel in comparison with the known time shifts in solid blue. We observe that significant errors and instability occur where the time shift sequence increases or decreases rapidly. Next the time of trace s_1 is shifted by $tshift_{est}(t)$ to get trace s_1^s and is plotted in solid blue in Figure 6 bottom panel, on top of which the reference trace s_2 is plotted again in dotted red. Where the estimated time shifts are obviously erroneous, trace s_1^s does not align with trace s_2.

The time-variant crosscorrelation coefficient at time τ between s_1^s and s_2 is calculated by

$$cc = (s_1^{s,\sigma} \otimes s_2^{\sigma})(t)|_{t=0} \quad (3)$$

where $s_1^{s,\sigma}$ is the time shifted trace s_1^s windowed by the same sliding Gaussian function as the one used to estimate the time-variant time shift sequence. Equation 3 means that trace s_1 after time shift and s_2 are windowed by the same sliding Gaussian function and the time-variant crosscorrelation coefficient corresponding to every Gaussian window center time is calculated between $s_1^{s,\sigma}$ and s_2^{σ} at the zero lag. Figure 6 middle panel exhibits the calculated time-variant crosscorrelation coefficient function, whose value is much lower than 1 where $tshift_{est}(t)$ is not accurate.

TVCC assumes that the time shifts are almost constant within every single Gaussian window. We have to choose a window width, which is small enough, but also has to be larger than the existing time shift to correctly calculate crosscorrelation coefficient. If the time shifts vary rapidly, a suitable window width may not exist and TVCC fails in estimating the time shifts. In this example, the known sinusoid time shift sequence has the maximum value of 30 ms. Figure 7 shows the case when its maximum value decreases to 10 ms and TVCC can estimate it precisely. Without windows, DTW or SDTW is more sensitive to the rapidly varying time shifts. Instead of estimating time shifts, this report employs TVCC to quantitatively examine the correlation between the synthetic seismogram and the seismic trace in the well tying procedure.

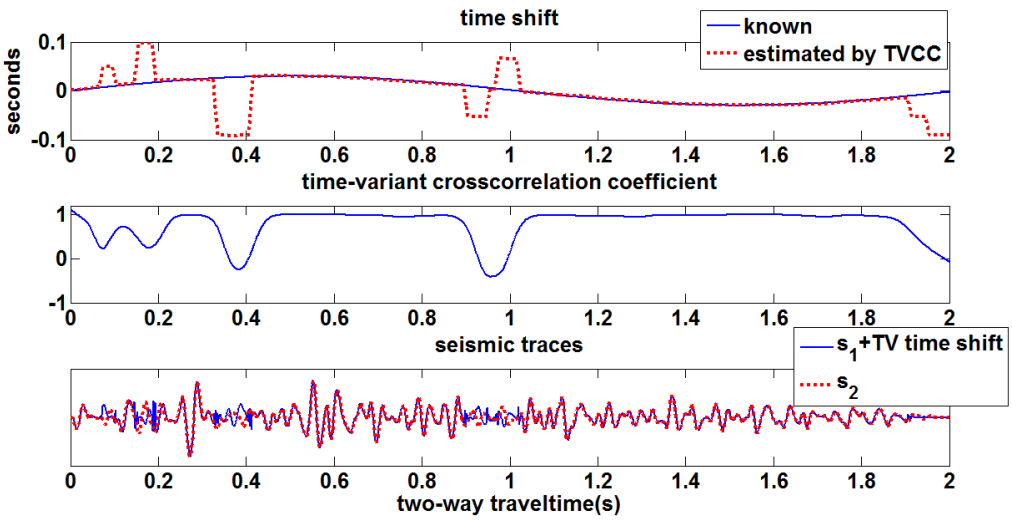

Figure 6: The known time shift sequence and its estimate (top). Time-variant crosscorrelation coefficient (middle). Time shifted s_1 compared to s_2 (bottom).

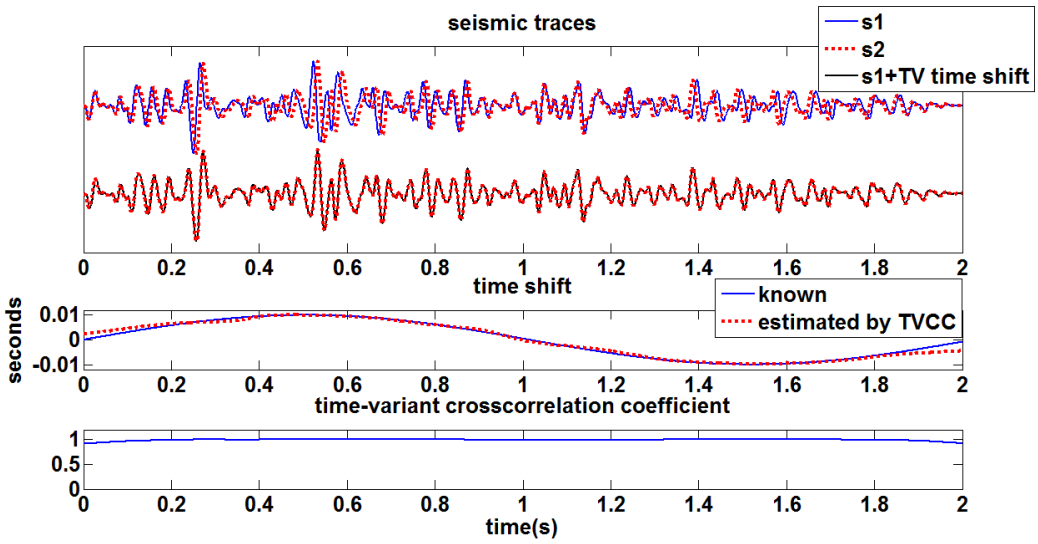

Figure 7: Trace s_1 before and after time-variant time shift estimated by TVCC compared to the reference trace s_2 (top). The known time-variant time shift function whose maximum value is **10** ms and its TVCC estimate (middle). Time-variant crosscorrelation coefficient (bottom).

SEISMIC-TO-WELL TIES ON HUSSAR FIELD DATA

In September 2011, CREWES initiated a seismic experiment near Hussar, Alberta, with the goal to study the low frequency content of the seismic data (Margrave et al., 2012). Figure 8 shows the location of the 4.5 km long seismic line and the three intersected wells 12-27, 14-27 and 14-35. While seismic datasets with different source and receiver types are available, this report uses the dataset with dynamite source recorded by 10 Hz geophones. P-wave sonic, density and gamma ray logs are available in all the three wells.

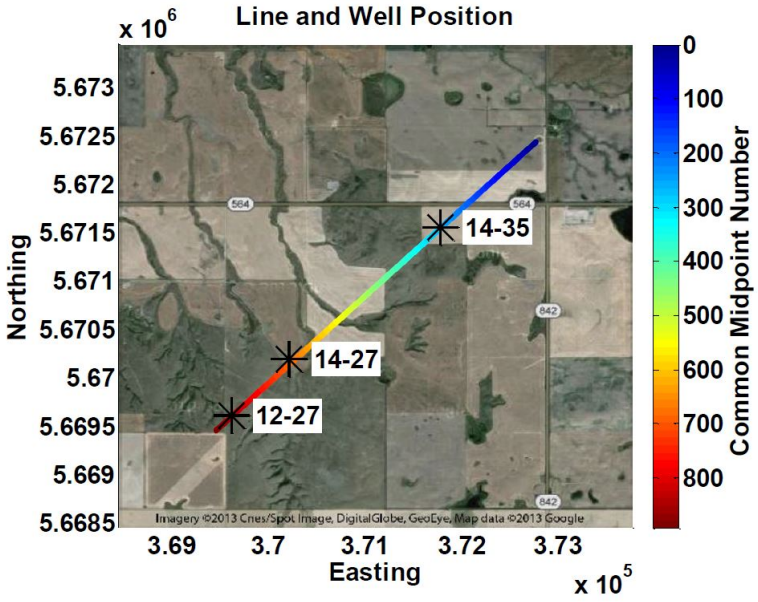

Figure 8: The location of the seismic line and wells in Hussar experiment (Lloyd, 2013).

Data preparation

The Hussar seismic data is processed through a flow of scaling and noise attenuation, spiking deconvolution, statics and velocity analysis, normal moveout removal, common depth point stack and migration (Lloyd, 2013). Figure 9 shows the fully processed zero-offset seismic section. At each well location, the nearest 5 seismic traces are averaged to tie the corresponding synthetic seismograms.

Figure 10 shows the density and p-wave velocity logs after a log editing process of removing null values, clipping unrealistic values and adding overburdens. Each overburden linearly extends the average value of the top 10 sonic or density log samples to the starting value at surface. The starting value for the density logs is 1500 kg/m^3 and that for the p-wave sonic logs is 1000 μs/m. Five tops called Basal Belly River, Base Fish Scales, Viking, Mannville and Medicine River Coal are denoted at the corresponding depth of each well, except that Medicine River Coal is missing at well 14-27. The subsurface structure is essentially flat in the Hussar area but the same tops appear deeper at well 12-27 than those of the other two wells. This is because the logs are measured with respect to the kelly bushing, whose elevation varies with the surface elevation and is significantly higher at well 12-27 than that at the other two wells (Margrave et al., 2012). In Figure 11, a normal incident p-wave reflectivity is calculated from each well and is plotted with respect to the two-way traveltime converted from the depth using the sonic log values.

Next a residual wavelet is estimated from each average trace by smoothing its amplitude spectrum and applying a zero phase (Cui and Margrave, 2014b). The residual wavelet is necessary to bandlimit the well reflectivity to the same frequency band of the seismic data. A zero-phase wavelet is symmetrical about time zero to make the maximum amount of energy in the wavelet be centered at the reflection coefficient, which is required by both

interpretation and impedance inversion. All the three estimated wavelets are plotted in Figure 12 and they look very similar to each other.

Convolving a well reflectivity with the zero-phase wavelet estimated at the well location, a synthetic seismogram is created and is compared to the corresponding average trace in Figure 13. Their events are not tied to each other and the overall crosscorrelation coefficient at lag zero is very small at each well location. Figure 14 plots the synthetic seismograms on the 2-D seismic section in the same gray level. The tops are denoted at the corresponding two-way traveltime converted from their depth using the sonic logs. We observe that none of the same well formations are tied to the same seismic events.

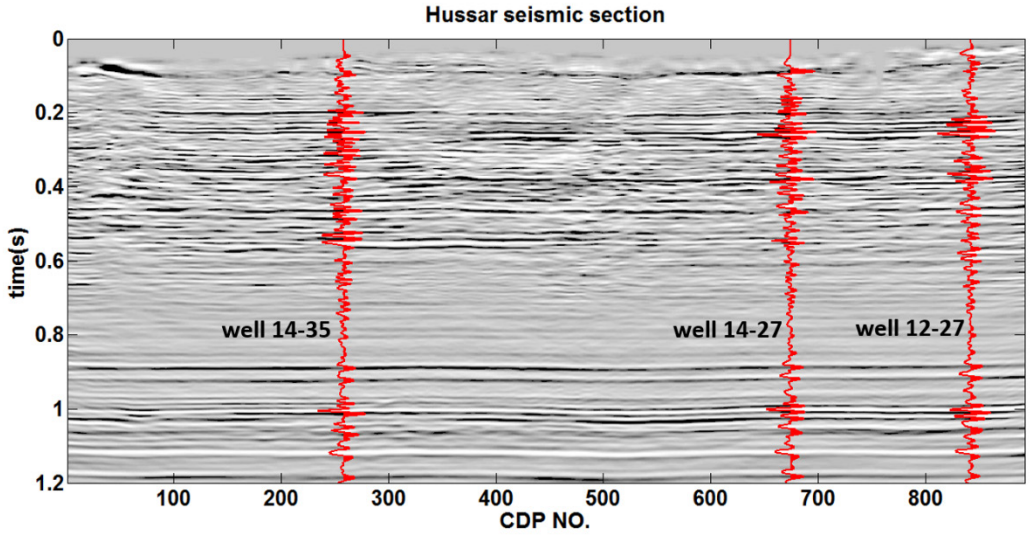

Figure.9: The 2-D seismic section after processing and migration. The three wiggle traces in red are the average traces at the corresponding well locations.

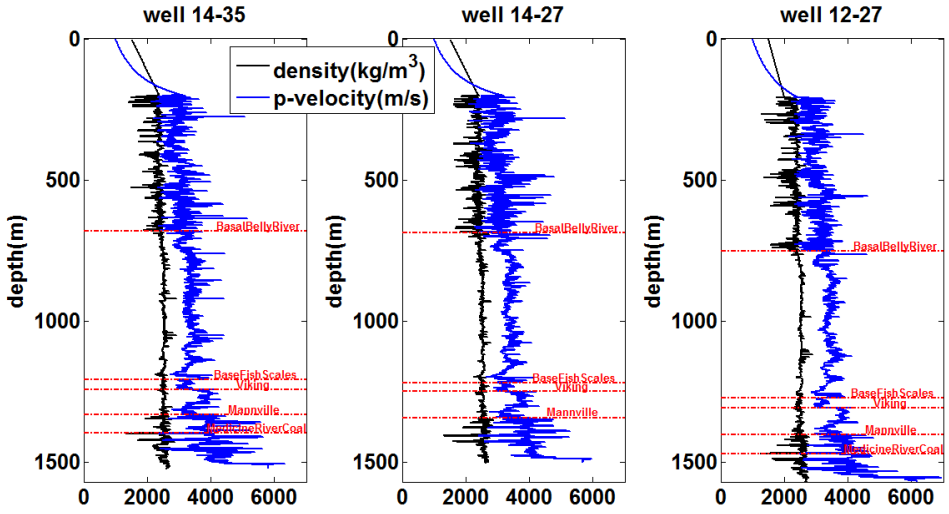

Figure 10: The density log and p-wave velocity log with the tops from each well after being edited.

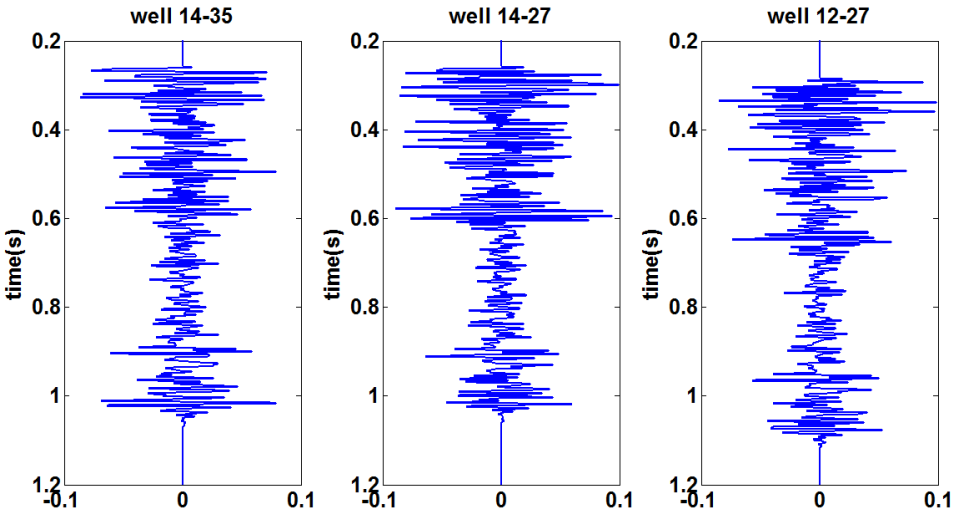

Figure 11: Reflectivity calculated from each well.

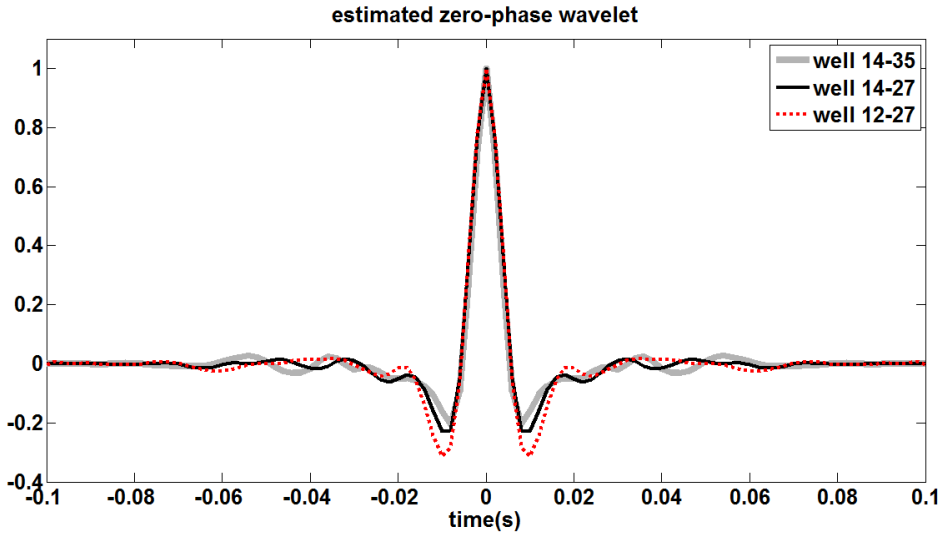

Figure 12: The zero-phase wavelet estimated from the average trace at each well location.

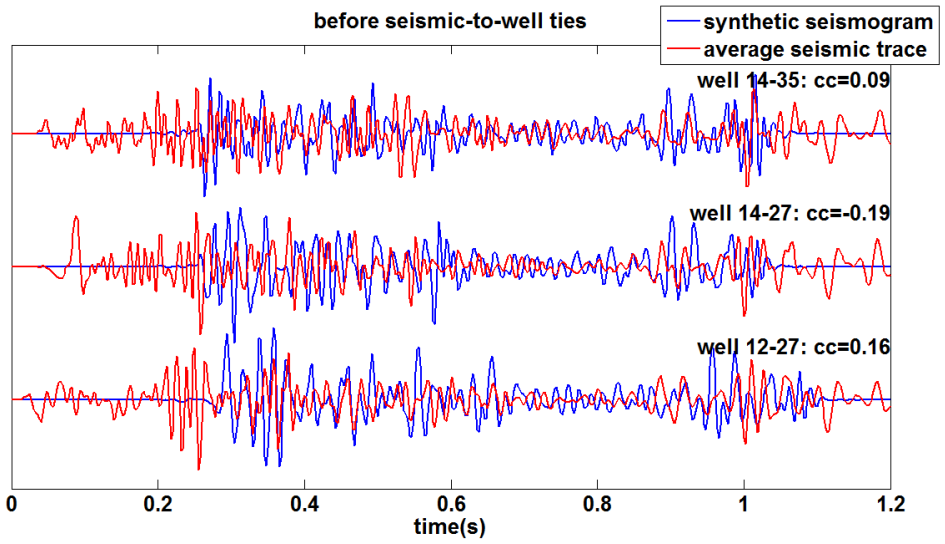

Figure 13: The synthetic seismogram and the average trace at the corresponding well location before being tied. The cc values annotated are their overall crosscorrelation coefficients at lag zero.

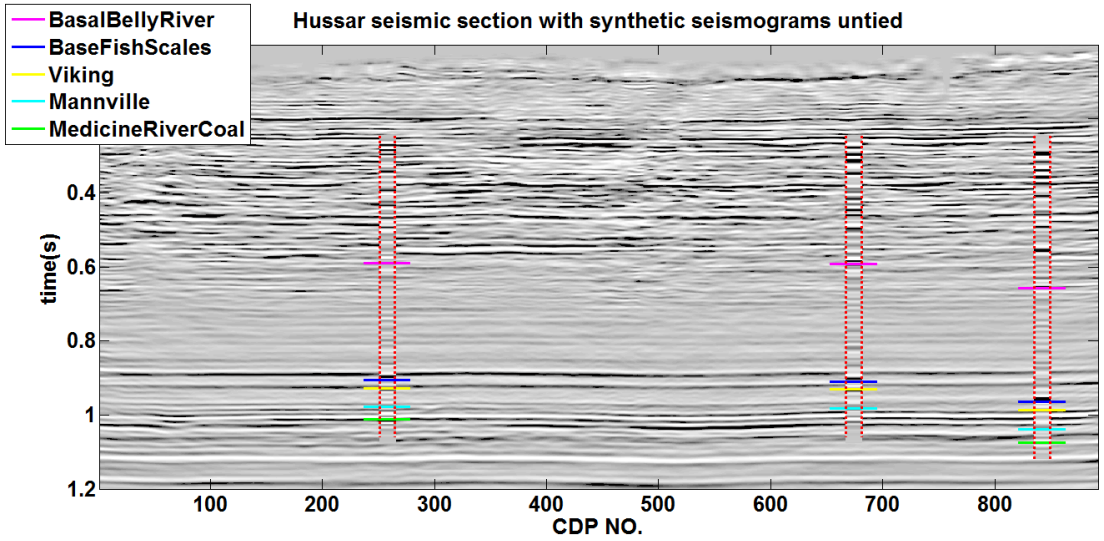

Figure 14: The 2-D seismic section, on top of which are the untied synthetic seismograms separated by the dotted red lines at the corresponding well locations with the tops annotated.

Seismic-to-wells

Without Q values or a check-shot/VSP survey available, SDTW is used to estimate the time shifts between the synthetic seismograms and the average seismic traces automatically. Figure 15 top panel shows the estimated time shifts using a coarse sample interval of 100 samples, namely 0.2 s. The time shifts are attributed to the combination of the residual drift time and overestimated sonic overburden, so they are all less than zero although they are getting larger with longer traveltime. The absolute values of the time shifts at well 12-27 are larger than those of the other two wells by a rough constant, resulting from the fact that its reference depth (the kelly bushing elevation) is higher than that of the other two wells.

The accuracy of the time shift estimation can be verified by the fact that all the three time shift sequences have similar slopes because of the flat subsurface geological features in the Hussar area.

The timing of each well reflectivity is corrected by the corresponding time shifts and is plotted on top of the original reflectivity in Figure 16. Convolving the time shifted reflectivity with the corresponding zero-phase residual wavelet in Figure 12, the reconstructed synthetic seismogram is plotted in Figure 17 compared to the corresponding average trace at each well location. Note that in this time calibration step, it is the timing of the well reflectivity that is being corrected instead of warping the original synthetic seismograms, so that their embedded zero-phase wavelets are not destroyed.

Next the time-variant constant-phase differences and amplitude scalar functions between the synthetic seismograms and the average traces in Figure 17 are calculated and plotted in Figure 15 middle and bottom panels. They are then linearly interpolated and extrapolated in the horizontal direction because of the flat subsurface properties in the Hussar area. The 2-D time-variant constant-phase and the 2-D time-variant amplitude scalar are plotted in Figure 18 and Figure 19 respectively. It can be seen that the traces near well 12-27 have relatively large phase errors at early times while the traces near well 14-27 have relatively large amplitude errors at middle times. Each seismic trace is phase rotated and amplitude balanced by the corresponding amounts. Since deconvolution is rarely perfect in its attempt to produce a zero-phase wavelet from the nonstationary minimum-phase wavelets, phase rotation is important to move the central peaks of the residual wavelets in the seismic traces to the position of the reflection coefficients. Figure 20 shows that the synthetic seismograms after time calibration are now tied to the 2-D seismic section after phase rotation and amplitude balancing very well. The same well tops tie to the same seismic event, making major seismic horizons easy to be identified. In Figure 21, the correlation of each pair of the synthetic seismogram and the average trace is shown to be much improved after well tying compare to Figure 13.

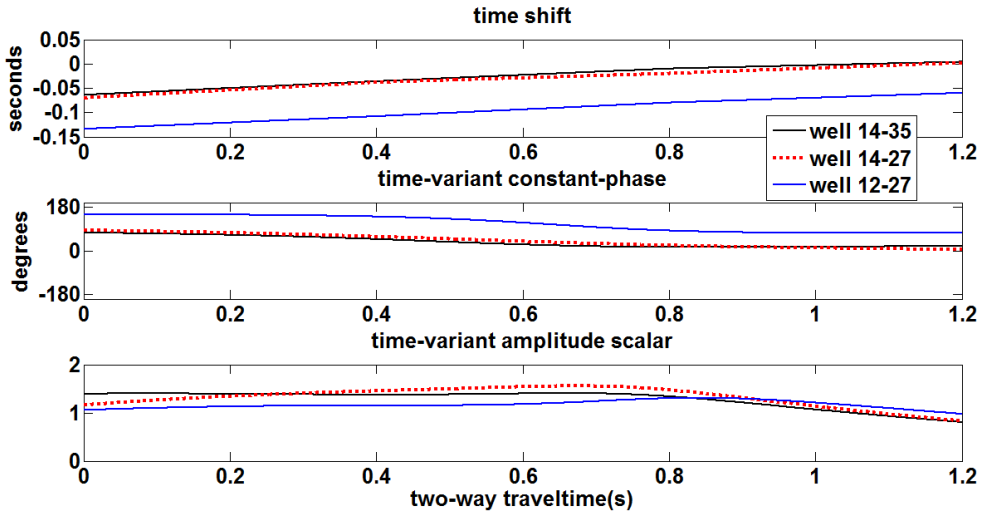

Figure 15: The time shifts between the average trace and the synthetic seismogram at the corresponding well location (top). The time-variant constant-phase difference between the average

trace and the synthetic seismogram after time calibration at each well location (middle). The time-variant amplitude scaler function between the phase rotated average trace and the synthetic seismogram after time calibration at each well location (bottom).

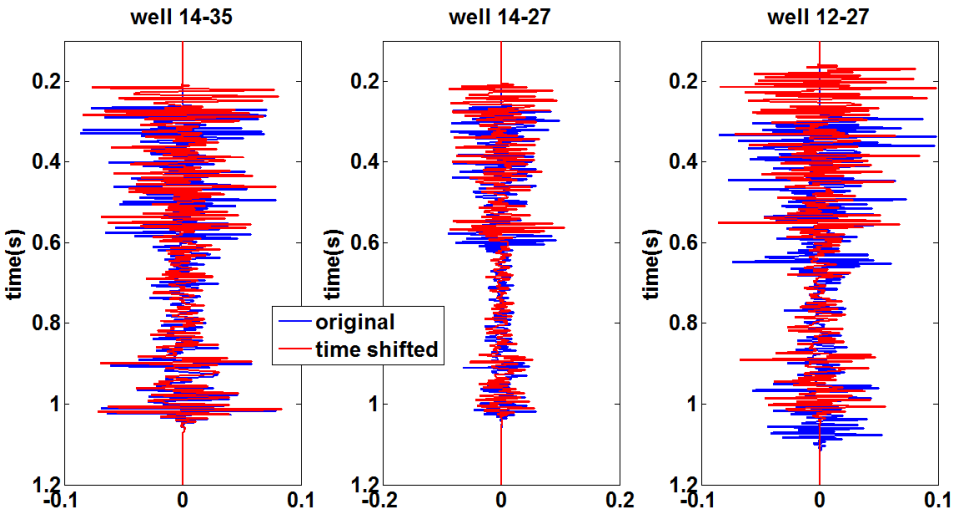

Figure 16: The original and time shifted reflectivities at each well.

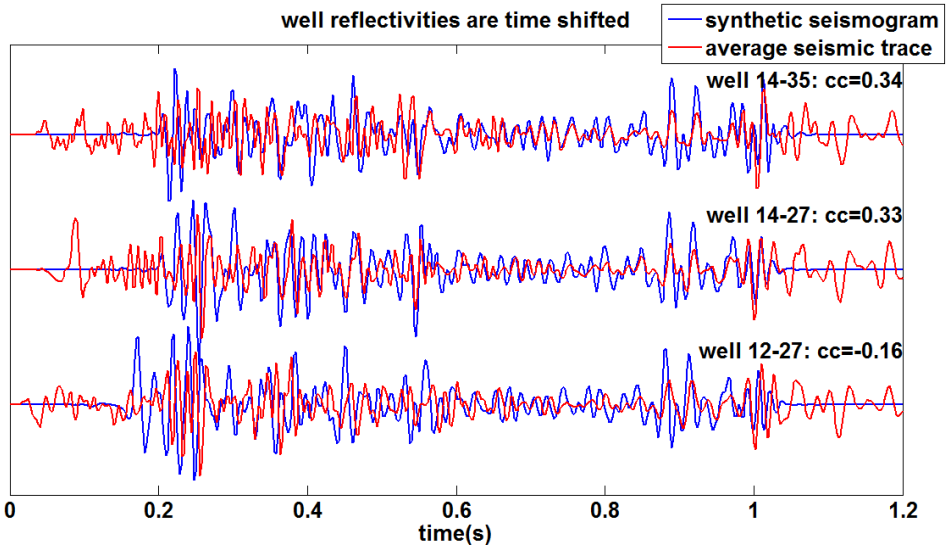

Figure 17: The reconstructed synthetic seismogram and the average trace at the corresponding well location after the timing of the reflectivity being corrected. The cc values annotated are their overall crosscorrelation coefficients at lag zero.

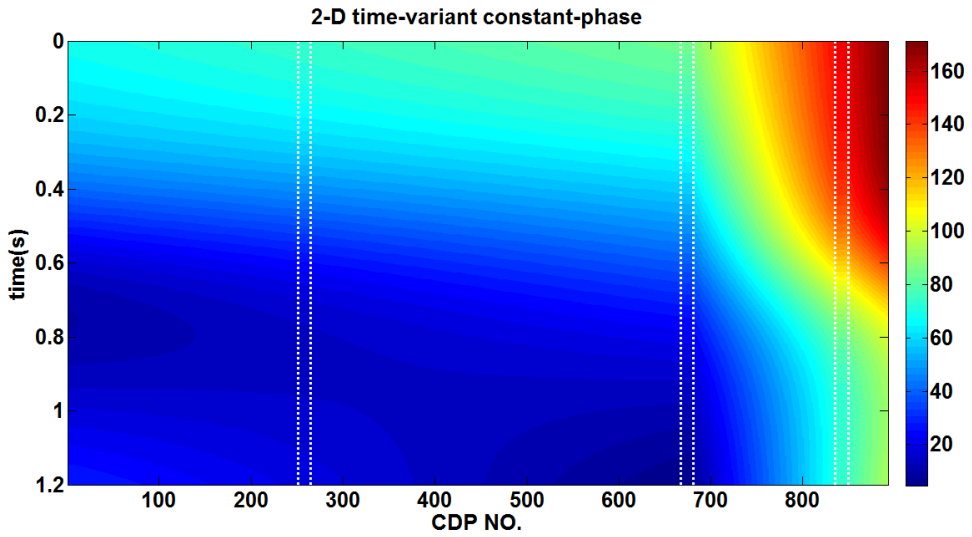

Figure 18: The 2-D time-variant constant-phase, on top of which are the phases used for interpolation and extrapolation at the corresponding well locations separated by the dotted white lines.

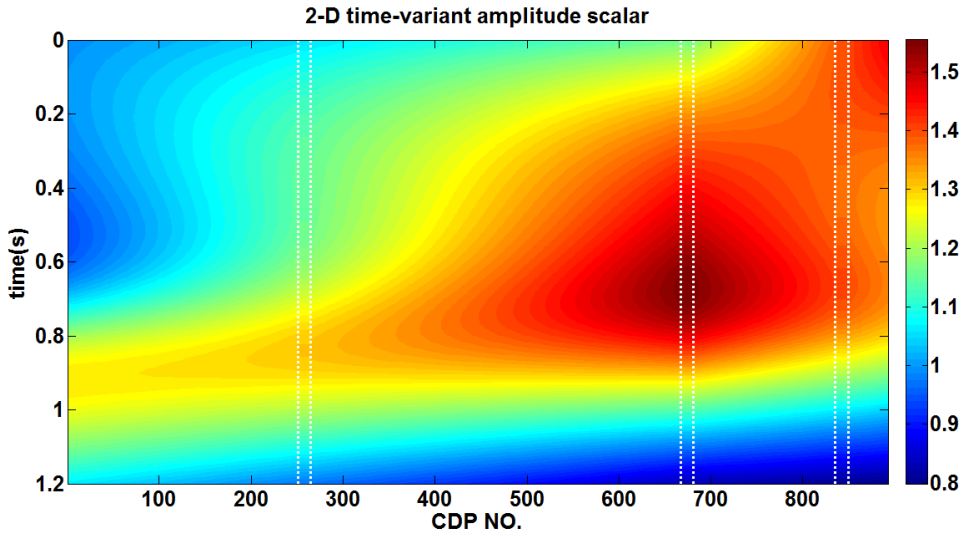

Figure 19: The 2-D time-variant amplitude scalar, on top of which are the scalars used for interpolation and extrapolation at the corresponding well locations separated by the dotted white lines.

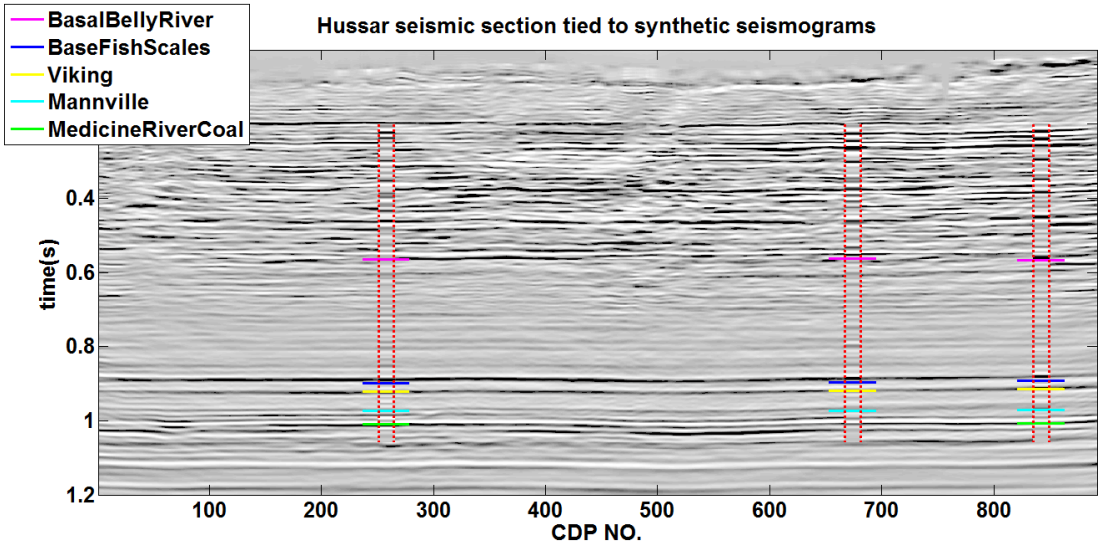

Figure 20: The 2-D seismic section after phase rotation and amplitude balancing, on top of which are the synthetic seismograms after time calibration at the corresponding well locations separated by the dotted red lines.

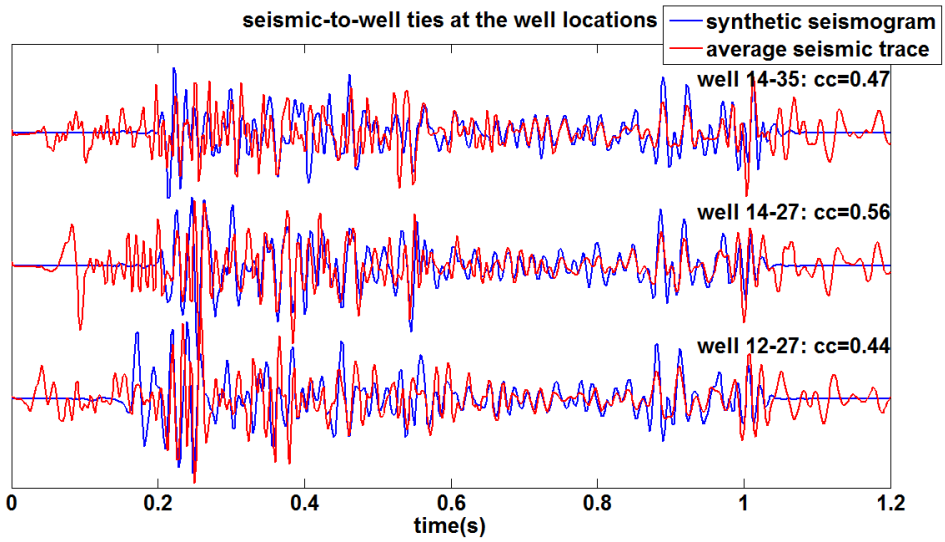

Figure 21: The synthetic seismogram and the average trace at the corresponding well location after being tied. The cc values annotated are their overall crosscorrelation coefficients at lag zero.

Bandlimited impedance inversion

Once the wells are tied to the seismic section, they can provide the low-frequency trend when the integrated seismic data is inverted into detailed impedance. The bandlimited impedance inversion (BLIMP) (Ferguson and Margrave, 1996) is a simple but powerful seismic inversion technique. The low frequency cut-off f_c and the high-end frequency f_h are two important parameters specified by the user. BLIMP estimates acoustic impedance

from a seismic trace of bandwidth from f_c to f_h combined with a log impedance of bandwidth below f_c.

The impedance of the three wells are calculated with respect to two-way traveltime after their timing is corrected by the SDTW estimated time shifts. Then the well impedance is linearly interpolated and extrapolated in the horizontal direction for the inversion of each trace in the 2-D seismic section. Figure 22 shows the 2-D interpolated well impedance section.

The low frequency cut-off f_c should be the lowest reliable seismic frequency. Selecting its value too low, the impedance inversion will contain noise from the seismic. Selecting its value too high will cause the seismic data to be overwritten with the well log information, causing subtleties in the seismic to be erased (Lloyd, 2013). To determine the optimal value of f_c, a series of frequency values ranging from 1 to 20 Hz in an increment of 0.5 Hz is tested. The trace at each well location is inverted using different testing values of f_c, the corresponding well impedance and a high-end frequency f_h of 75 Hz. The 2-norm errors are calculated between each seismic impedance inversion and the corresponding low-pass filtered log impedance using $f_h = 75$ Hz, and are plotted in Figure 23 with respect to the values of f_c. The errors drop rapidly with an increasing f_c and become stably small at about 3 Hz for the three wells, so 3 Hz is chosen as the optimal low frequency cut-off. Figure 24 shows the bandlimited impedance inversion of the 2-D seismic section using $f_c = 3$ Hz and $f_h = 75$ Hz, which is roughly consistent with the low-pass filtered log impedance at each well location. To qualitatively evaluate the accuracy of the seismic impedance inversion, Figure 25 compares the low-pass filtered log impedance I_{well} with the bandlimited seismic impedance inversion $I_{inversion}$ at the corresponding well location. Their percent error is calculated by

$$error = \frac{norm(I_{inversion} - I_{well})}{norm(I_{well})} \times 100 \qquad (4)$$

where $norm$ is the 2-norm. It can be noticed that the percent error is relatively high at well 12-27 compared to the other two wells.

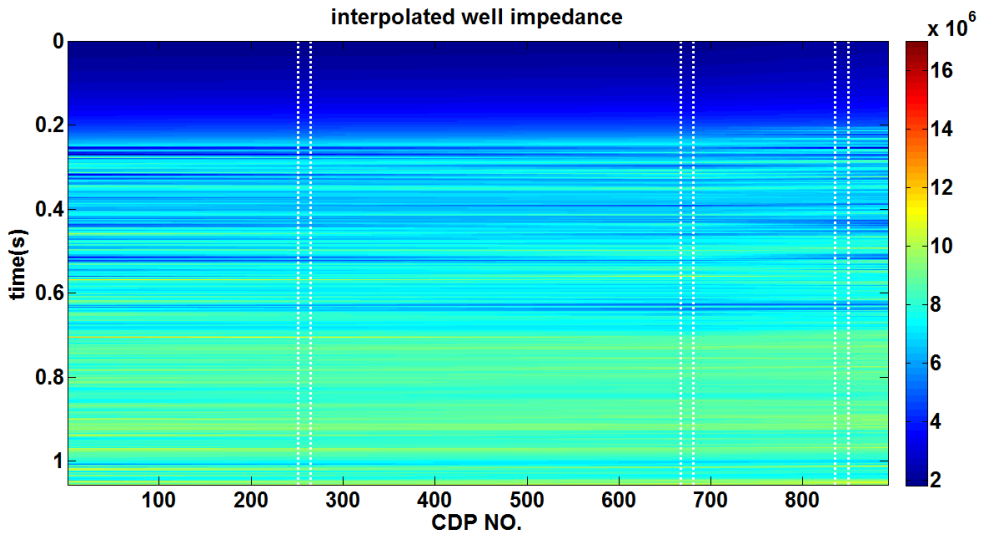

Figure 22: The 2-D interpolated well impedance section, on top of which are the well impedance used for interpolation and extrapolation at the corresponding well locations separated by the dotted white lines.

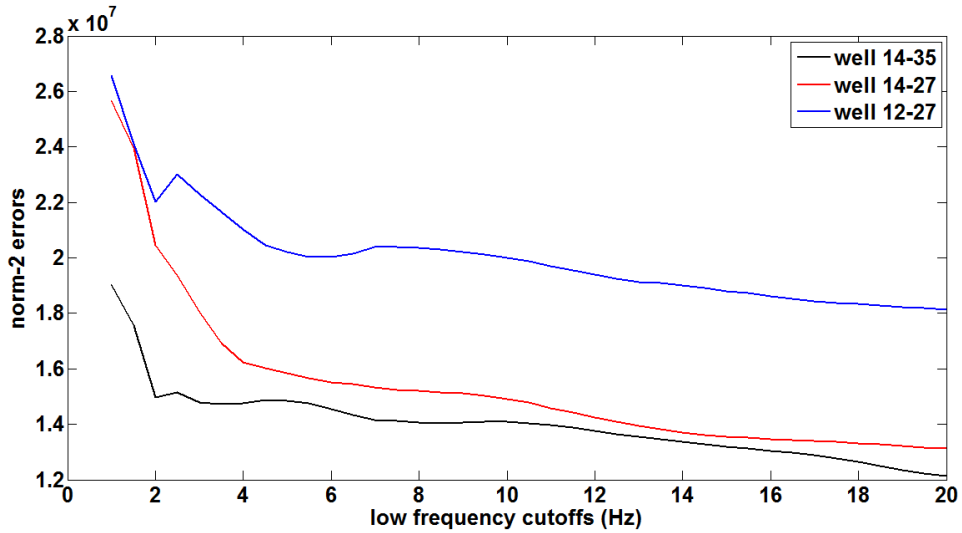

Figure 23: The norm-2 errors between the log impedance and the impedance inversion of the seismic trace at each well location using different low frequency cut-offs.

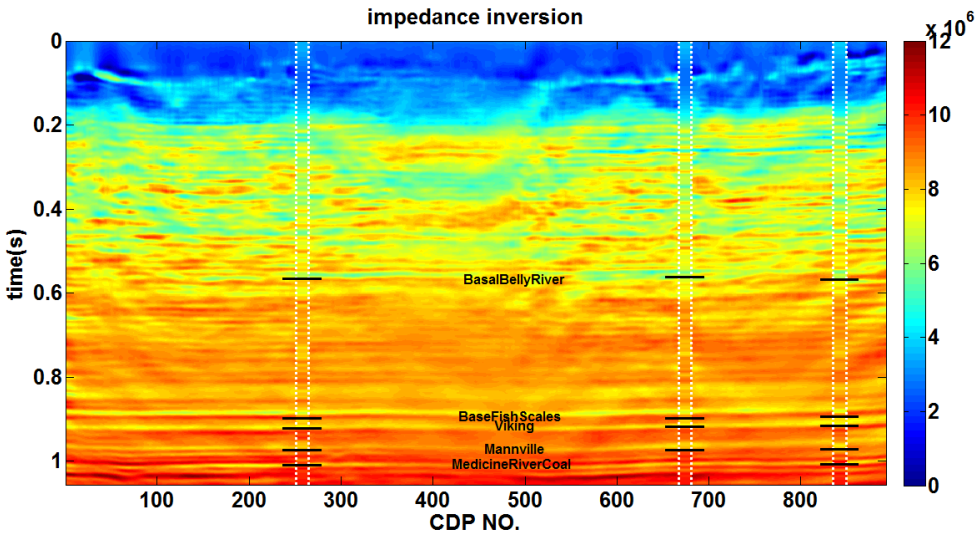

Figure 24: Bandlimited impedance inversion of the 2-D seismic section, on top of which are the low-pass filtered well impedance separated by the dotted white lines at the corresponding well locations with the tops annotated.

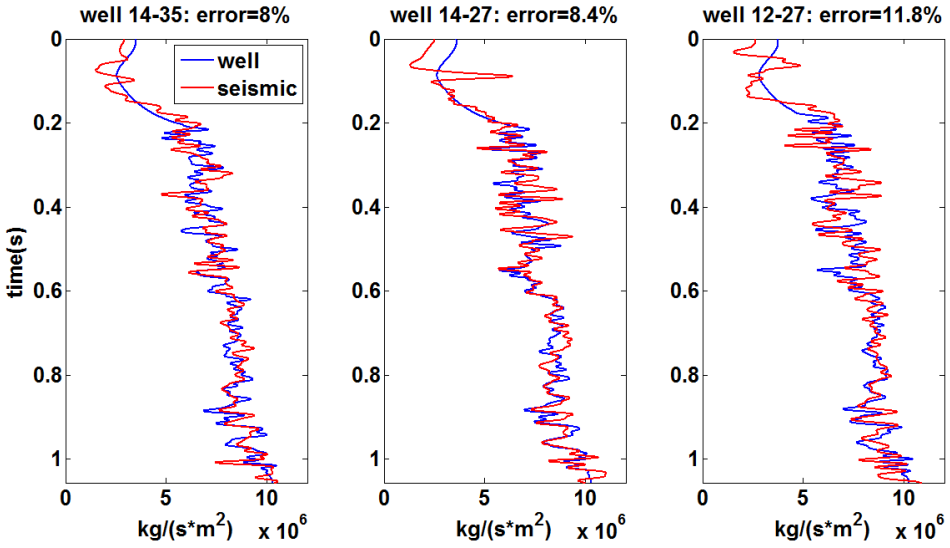

Figure 25: Comparison of the low-passed well impedance and the bandlimited seismic impedance inversion at each well location with their percent errors denoted.

Discussion

As is seen from the 2-D time-variant constant-phase section in Figure 18, the phase values are anomalously large around well 12-27. It is unrealistic to rotate the seismic traces by such large phase angles. The phase anomaly may be an indication of insufficient time shift correction of well 12-27 since its reference depth level is higher than that of the other two wells. To verify this guess, a second iteration of time calibration process is applied. The time shifts between the previously time corrected synthetic seismogram and the average seismic trace at each well location in Figure 17 are estimated by SDTW again and

are plotted in Figure 26 top panel. Noticeable time shift amounts are detected even after the first iteration of time calibration, especially at well 12-27. Next, the timing of the reflectivity is further corrected by these time shifts again to construct the synthetic seismogram with twice time calibration, whose time-variant constant-phase difference with the average trace at each well location is calculated and plotted in Figure 26 middle panel. The phase is smaller than that in the first iteration shown in Figure 15 middle panel, indicating that an inadequate time shift correction can bias the following constant-phase estimation. A third iteration of time calibration is employed in the same way and the results are shown in Figure 27. The time shifts are all reduced to zero and the time-variant constant-phase difference is the same as that in the second iteration, verifying that the timing of the three wells is sufficiently corrected after two iterations. The reason why time calibration in this case needs several iterations to converge may be that the SDTW estimated time shifts are used to correct the timing of the reflectivity instead of warping the synthetic seismogram, the latter of which is required by the objective of the SDTW algorithm, making this optimization problem nonlinear.

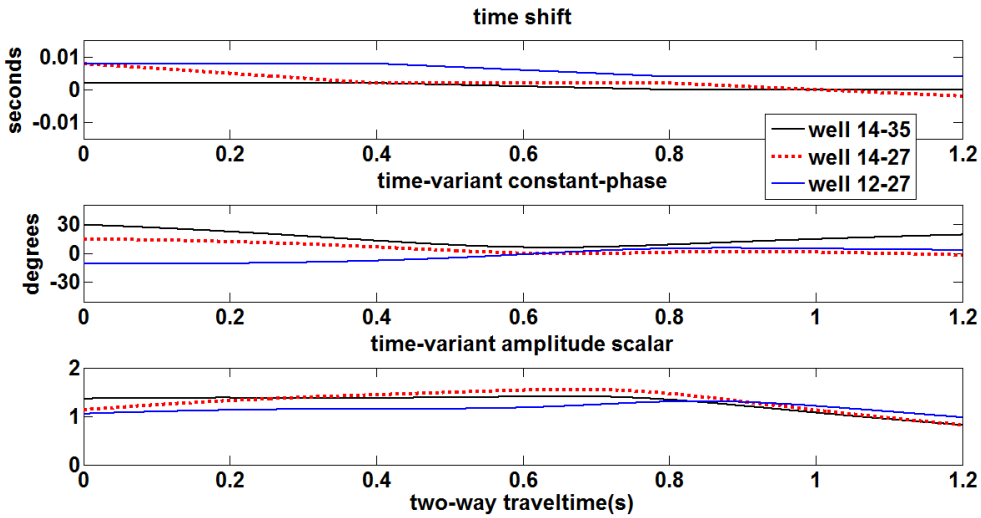

Figure 26: The results in the second iteration of time calibration are shown. The time shifts between the average trace and the synthetic seismogram after time calibration once (top). The time-variant constant-phase difference between the average trace and the synthetic seismogram after time calibration twice (middle). The time-variant amplitude scaler function between the phase rotated average trace and the synthetic seismogram after time calibration twice (bottom).

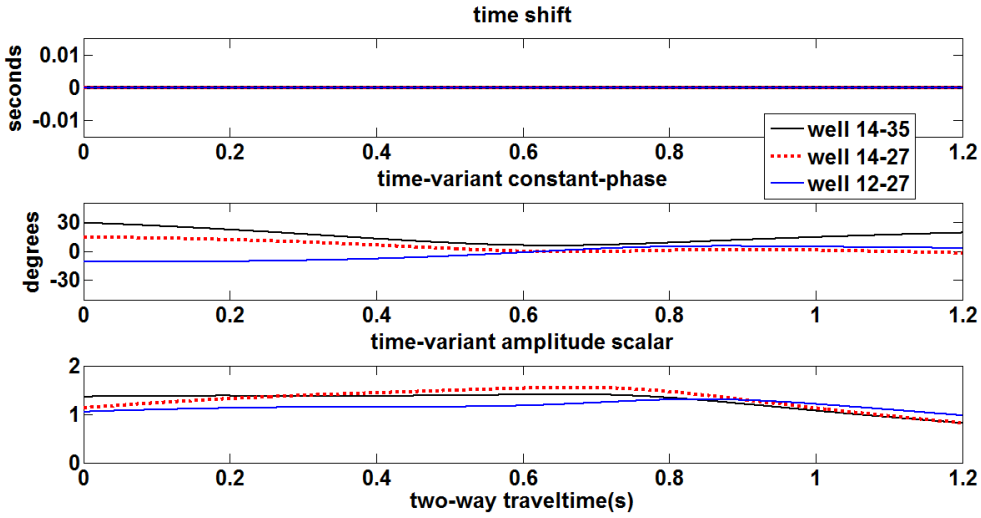

Figure 27: The results in the third iteration of time calibration are shown. The time shifts between the average trace and the synthetic seismogram after time calibration twice (top). The time-variant constant-phase difference between the average trace and the synthetic seismogram after time calibration three times (middle). The time-variant amplitude scaler function between the phase rotated average trace and the synthetic seismogram after time calibration three times (bottom).

After two iterations, the time-variant constant-phase difference (Figure 26 or Figure 27 middle panel) and the time-variant amplitude scalar (Figure 26 or Figure 27 bottom panel) at three well locations are linearly interpolated and extrapolated in the horizontal direction, shown in Figure 28 and Figure 29 respectively. The phase values are much smaller than those in the first iteration in Figure 18 while the 2-D amplitude scalar section is almost the same as Figure 19. The seismic traces are phase rotated and amplitude balanced by the amount calculated in the second iteration and the final 2-D seismic section is displayed in Figure 30, on top of which are the synthetic seismograms after time calibration twice. The well tying result is visually similar to that with only one iteration of time calibration as shown in Figure 20. Each pair of the tied synthetic seismogram and the average trace is plotted in Figure 31 and their overall crosscorrelation coefficients are all increased from the first iteration in Figure 21. The time-variant crosscorrelation coefficients between the synthetic seismogram and the seismic trace before well tying, after well tying with time calibration once and after well tying with time calibration twice are calculated using Equation 3 and are plotted in Figure 32 for each well location, showing that the second iteration of time calibration considerably improves the well tying at early times for well 12-27.

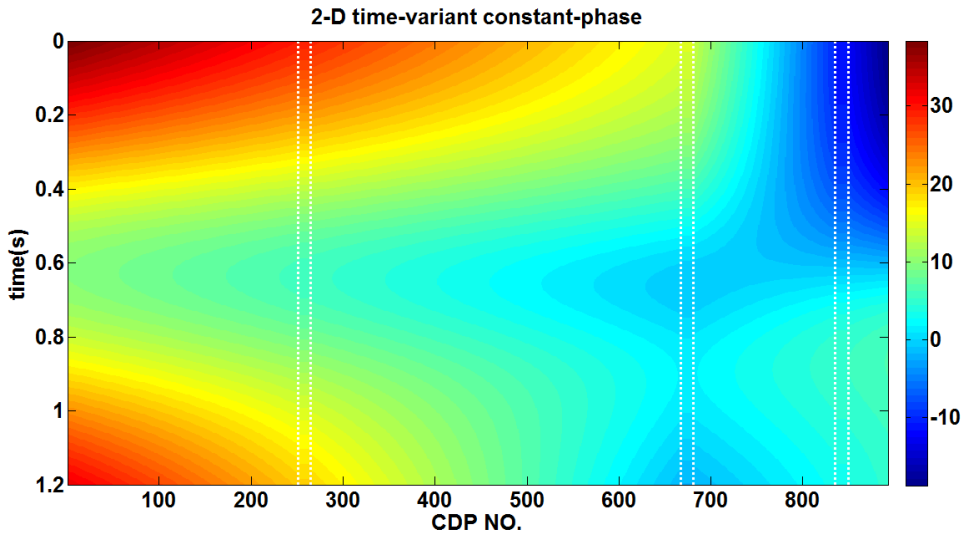

Figure 28: The 2-D time-variant constant-phase after two iterations, on top of which are the phases used for interpolation and extrapolation at the corresponding well locations separated by the dotted white lines.

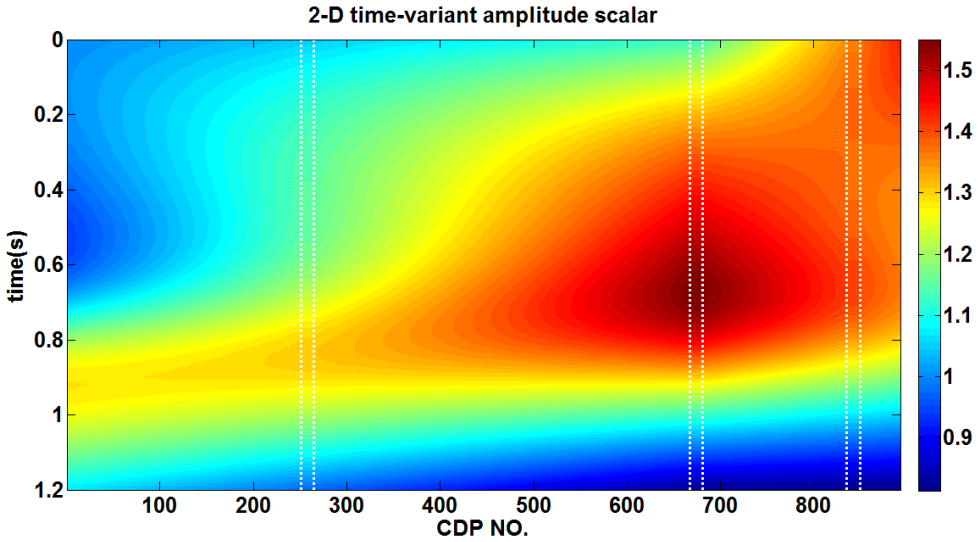

Figure 29: The 2-D time-variant amplitude scalar after two iterations, on top of which are the scalars used for interpolation and extrapolation at the corresponding well locations separated by the dotted white lines.

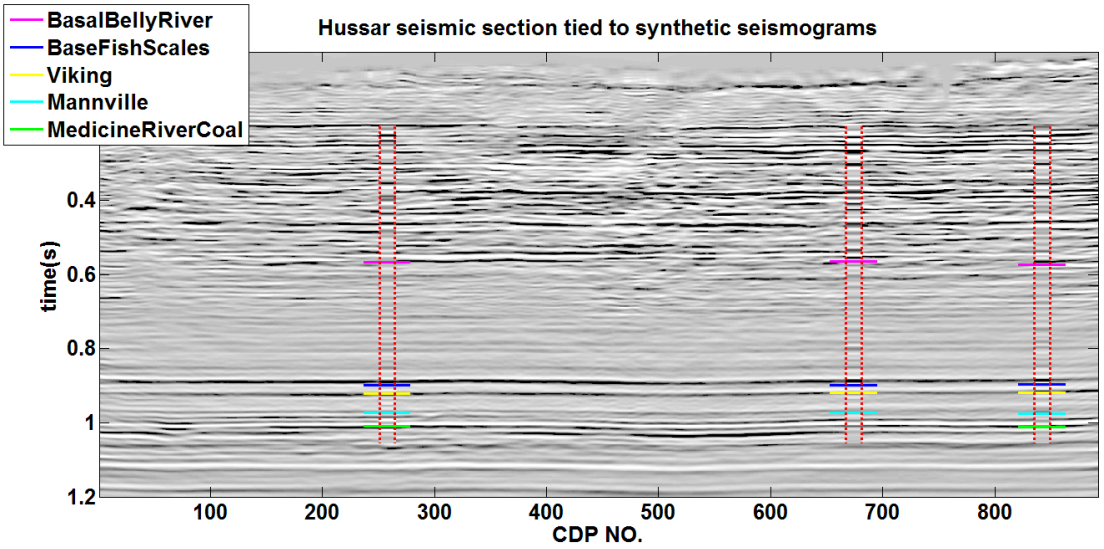

Figure 30: The final well tying results after two iterations of time calibration are shown. The 2-D seismic section after phase rotation and amplitude balancing, on top of which are the synthetic seismograms after time calibration twice at the corresponding well locations separated by the dotted red lines.

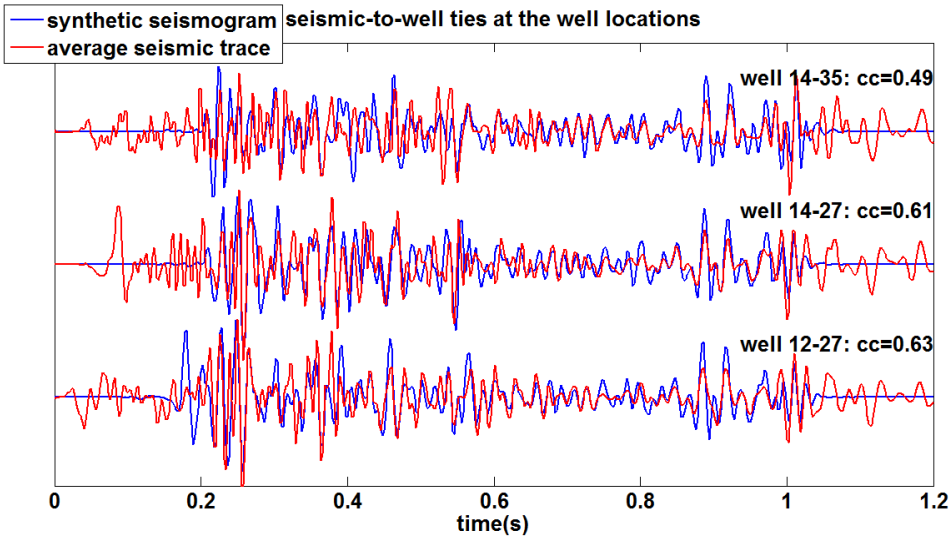

Figure 31: The synthetic seismogram and the average trace at the corresponding well location after being tied through two iterations of time calibration. The cc values annotated are their overall crosscorrelation coefficients at lag zero.

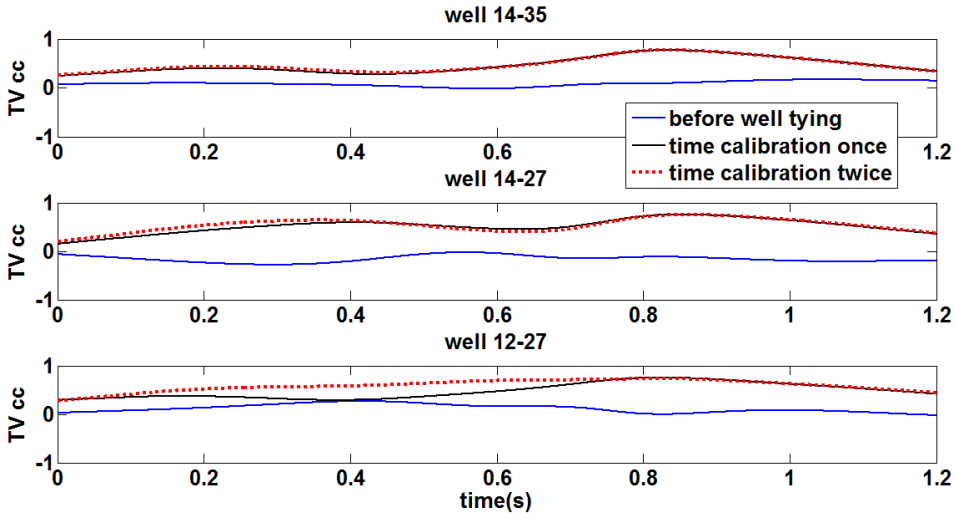

Figure 32: The time-variant crosscorrelation coefficients between the synthetic seismogram and the seismic trace before well tying, after well tying with time calibration once and after well tying with time calibration twice.

With the wells tied to the seismic section after two iterations of time calibration, the seismic data is inverted to the bandlimited impedance shown in Figure 33 using the same values of f_c and f_h. Figure 34 also compares the percent error between the low-pass filtered log impedance with the bandlimited seismic impedance inversion at each well location using Equation 4. The error is slightly higher at well 14-35 while is lower at well 14-27 and well 12-27 than that with well tying of one time calibration iteration. Similarly, the impedance percent error is calculated between the seismic impedance inversion and the interpolated well impedance at every CDP location. Figure 35 compares the errors with one and two iterations of time calibration in the well tying. The second iteration is seen to bring down the errors significantly around well 12-27, verifying better seismic-to-well ties.

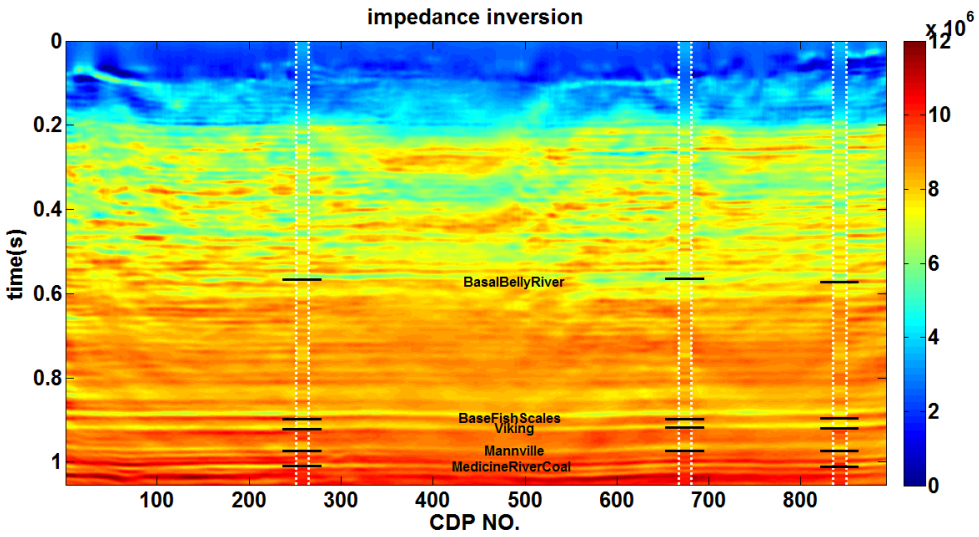

Figure 33: Bandlimited impedance inversion of the 2-D seismic section, with two iterations of time calibration in the well tying, on top of which are the low-pass filtered well impedance separated by the dotted white lines at the corresponding well locations with the tops annotated.

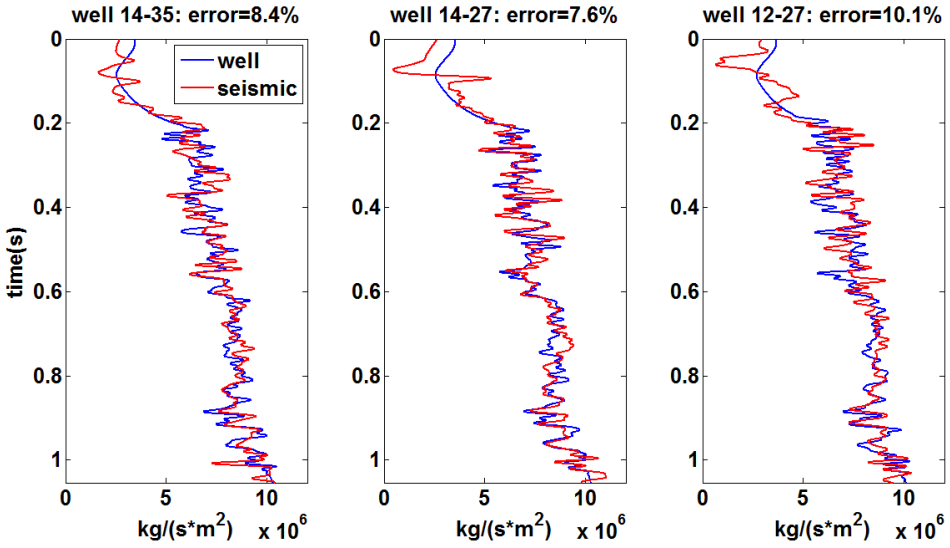

Figure 34: Comparison of the low-passed well impedance and the bandlimited seismic impedance inversion with two iterations of time calibration in the well tying. Their impedance percent errors are denoted.

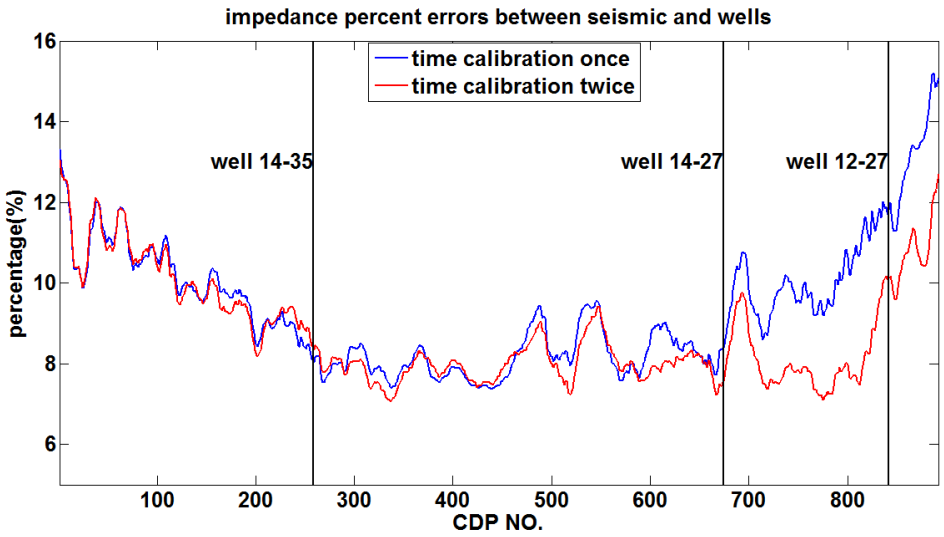

Figure 35: The impedance percent errors between the seismic impedance inversion and the interpolated well impedance at every CDP location, with one and two iterations of time calibration in the well tying.

CONCLUSIONS

Smooth dynamic time warping (SDTW) can accurately estimate smooth time shifts between two signals automatically, which are more realistic to represent the drift time in seismic-to-well ties than those estimated by dynamic time warping (DTW). Smoothing the rough time shifts estimated by DTW is not equal to the globally optimal time shifts computed by SDTW. Dynamic time warping or smooth dynamic time warping is more sensitive to the rapidly varying time shifts than time-variant crosscorrelation.

Without knowledge of Q, a check-shot/VSP survey or manually stretching or squeezing the synthetic seismogram, SDTW can estimate the time shifts between the synthetic seismogram and the seismic trace for the Hussar data. The time shifts are attributed to the combination of the residual drift time and overestimated sonic overburden, and they have similar slopes at all the three well locations. The fact that the subsurface geological structure is flat in the Hussar area validates the time shift estimation as well as the linear interpolation and extrapolation of the time-variant constant-phase and the time-variant scalar from the well locations to other CDP locations horizontally.

The estimated time shifts are used to calibrate the timing of the reflectivity, instead of warping the synthetic seismogram required by the objective of the SDTW algorithm, to reserve the embedded zero-phase wavelets but making this optimization problem nonlinear and converge only after several iterations. For this Hussar dataset, the first iteration of time calibration is not sufficient, leading to a constant-phase estimation bias. After two iterations, the time shifts are adequately corrected and the constant-phase difference is reasonably small.

After seismic-to-well ties, the same well tops are tied to the same seismic events, making major seismic horizons easy to be identified. The correlation of the synthetic seismogram and the average trace at each well location is much increased compared to that before well

tying. The bandlimited impedance inversion of the Hussar seismic data using a low-frequency cut-off of 3 Hz and a high-end frequency of 75 Hz is shown to be a good approximation to the subsurface properties. The second iteration of time calibration significantly reduces the percent errors around well 12-27 between the seismic inversion and well impedance, verifying better seismic-to-well ties.

ACKNOWLEDGEMENTS

The authors thank the sponsors of CREWES for continued support. This work was funded by CREWES industrial sponsors and NSERC (Natural Science and Engineering Research Council of Canada) through the grant CRDPJ 461179-13. Author 1 was also supported by scholarships from the SEG Foundation and the Department of Geoscience at the University of Calgary.

REFERENCES

Compton, S., and Hale, D., 2014, Estimating V-P/V-S ratios using smooth dynamic image warping: Geophysics, 79, V201-V215.

Cui, T., and Margrave, G. F., 2014a, Drift time estimation by dynamic time warping: CREWES Research Report, 26.

Cui, T., and Margrave, G. F., 2014b, Seismic wavelet estimation: CREWES Research Report, 26.

Ferguson, R. J., and Margrave, G. F., 1996, A simple algorithm for bandlimited impedance inversion: CREWES Research Report, 8.

Lloyd, H. J. E., 2013, An investigation of the role of low frequencies in seismic impedance inversion: M.Sc. thesis, University of Calgary.

Margrave, G. F., Mewhort, L., Phillips, T., Hall, M., Bertram, M. B., Lawton, D. C., Innanen, K. A. H., Hall, K. W., and Bertram, K. L., 2012, The Hussar low-frequency experiment: CSEG Recorder, September, 25-39.